

Modulation of the Sorption Characteristics for an H-bonded porous Architecture by Varying the Chemical Functionalization of the Channel Walls

Nans Roques,^{*,[a]} Anthony Tovar-Molle,^[a] Carine Duhayon,^[a] Stéphane Brandès,^[b] Alex Spieß,^[c] Christoph Janiak,^[c] and Jean-Pascal Sutter^{*,[a]}

Abstract: Five isostructural microporous supramolecular architectures prepared by H-bonded assembly between the hexa-anionic complex $[\text{Zr}_2(\text{Ox})_7]^{6-}$ (Ox = oxalate, $(\text{C}_2\text{O}_4)^{2-}$) and tripodal cations $(\text{H}_3\text{-TripCH}_2\text{-R})^{3+}$ with R = H, CH_3 , OH and OBn (Bn = CH_2Ph) are reported. The possibility to obtain the same structure using a mixture of tripodal cations with different R group (R = OH and R = CH_3) has also been successfully explored, providing a unique example of three-component H-bonded porous framework. The resulting SPA-1(R) materials feature 1D pores decorated by R groups, with apparent pore

diameters ranging from 3.0 to 8.5 Å. Influence of R groups on the sorption properties of these materials is evidenced through CO_2 and H_2O vapor sorption/desorption experiments, as well as with I_2 capture/release experiments in liquid media. This study is one of the first to demonstrate the possibility of tuning the porosity and exerting precise control over the chemical functionalization of the pores in a given H-bonded structure, without modifying the topology of the reference structure, and thus finely adjusting the sorption characteristics of the material.

Introduction

Hydrogen-bonded (H-bonded) porous materials (also known as HOFs when purely organic) are a rising class of porous molecular architectures^[1] for which properties typical of porous solids (sorption for storage^[2] or sequestration,^[3] heterogeneous catalysis,^[4–5] gas separation and purification^[6–7]) and of molecular functional materials (sensing,^[8–9] proton and/or semiconductors,^[10–11] photoluminescence,^[12] biological applications,^[13] among numerous others^[14–16]) have been evidenced and investigated. Although the number of reports concerning these architectures has considerably increased in

recent years,^[17–20] only a limited attention has been directed to the modulation of the pore size and/or sorption properties of a given framework.^[13,21–25] In the reported examples, pore expansion with retention of the network topology is obtained by insertion of rigid arms between the molecule core and functional groups able to form predictable H-bonds (imide,^[21] benzimidazolone,^[21] pyrazole,^[22] carboxylic acid).^[13,23–25]

The use of H-bonds as supramolecular “cement” to assemble organic molecules generally results in highly crystalline (and regenerable) solids due to the reversible nature of these bonds.^[1] However, H-bonds are weaker than coordination and covalent bonds, and are complemented by additional supramolecular interactions (π - π interactions, halogen-bonds, ...), making it difficult to predict and control the framework topology. A small alteration of the organic component involved in a HOF often results in structural changes rather than a modulation of the porosity for the resulting material. It is even more difficult to tune the chemical groups located in the pore walls to adjust the sorption characteristics or pores size. HOFs combining tunable pore sizes and characteristics are very scarce. A remarkable example is the series of 25 isostructural H-bonded frameworks based on the same sophisticated steroidal urea reported by Natarajan, Davis et al.^[26–27] This flexibility was attributed to the combination of urea H-bond donor-acceptor groups on the rigid steroidal scaffold; these act as a robust assembly algorithm directing the formation of the same supramolecular framework. Another modifiable HOF is a dipeptide-based architecture; however, porous structures are only formed with specific amino acid units, which limits the versatility of pore alterations.^[28–30]

The ability to tune porosity and exert precise control over the size and chemical functionalization of pores in a given H-

[a] Dr. N. Roques, A. Tovar-Molle, Dr. C. Duhayon, Dr. J.-P. Sutter
Laboratoire de Chimie de Coordination du CNRS (LCC-CNRS)
Université de Toulouse
CNRS, F-31077 Toulouse (France)
E-mail: nans.roques@lcc-toulouse.fr
jean-pascal.sutter@lcc-toulouse.fr

[b] Dr. S. Brandès
Institut de Chimie Moléculaire de l'Université de Bourgogne (ICMUB, UMR
CNRS 6302)
Université Bourgogne Franche-Comté
9 Avenue Alain Savary, F-21078 Dijon (France)

[c] A. Spieß, Prof. Dr. C. Janiak
Institut für Nanoporöse und Nanoskalierte Materialien
Heinrich-Heine-Universität Düsseldorf
D-40225 Düsseldorf (Germany)

Supporting information for this article is available on the WWW under
<https://doi.org/10.1002/chem.202201935>

© 2022 The Authors. Chemistry - A European Journal published by Wiley-VCH GmbH. This is an open access article under the terms of the Creative Commons Attribution Non-Commercial NoDerivs License, which permits use and distribution in any medium, provided the original work is properly cited, the use is non-commercial and no modifications or adaptations are made.

bonded framework, without altering the topology of the reference structure, thus remains an ambitious goal. For comparison, this is classically achieved for Metal–Organic Frameworks (MOFs)^[31–34] or Covalent Organic Frameworks (COFs),^[35–36] to adjust the sorption, storage and/or separation properties. Herein we show that chemical tuning of the pore walls is also possible in H-bonded porous materials.

While most of the H-bonded porous materials are formed with neutral molecules, an alternative strategy to achieve such architectures is based on ionic building-blocks with complementary charges. In this case, the supramolecular assembly relies on ionic/charge-assisted H-bonds known to be much stronger than a conventional H-bond.^[37] Inspired by the seminal work of Ward et al. on low density guanidinium sulfonates frameworks,^[38] related materials involving carboxylates and/or amidinium, ammonium or pyridinium have been described,^[39–43] showing that rational framework design, guest exchange and/or selective encapsulation are possible in these supramolecular architectures.^[44–45] The same approach can be implemented with ionic metal complexes.^[46–48] Several examples of open-framework architectures,^[49–51] including some porous frameworks,^[39,52–55] have been reported. Along this line, our approach involves negatively-charged metal complexes, such as metal-oxalate or analogues, acting as H-bond acceptors^[56–57] towards H-bond donor organic cations to form networks underpinned by robust and reliable supramolecular synthons. The organic units are designed to possess a given charge, geometry, and H-bond donor sites (ex. guanidinium,^[57] amidinium,^[58] ammonium,^[49,58] imidazolium,^[39,59–60] or pyridinium^[61–63]). Supramolecular porous architectures (SPA hereafter) with large pores have been achieved, including a material with channels decorated by basic pyridyl groups

capable to efficiently adsorb acidic molecules,^[62] or to template the growth of metal nanoparticles.^[63] In the course of these investigations, a SPA with very robust structure, showing 1D channels (*ca.* 8.5 Å of apparent diameter), has been identified.^[61] This solid, SPA-1(H), results from the 2:1 assembly between $[\text{H}_3\text{-TripCH}_2\text{-R}]^{3+}$ tripodal cations with $\text{R}=\text{H}$ and $[\text{Zr}_2(\text{Ox})_7]^{6-}$ complexes ($\text{Ox}=(\text{C}_2\text{O}_4)^{2-}$, Scheme 1). We now report that the large space available in the channels permits varying the R group of the organic units without compromising the topology of the H-bonded network. Isostructural SPA-1(R), where $\text{R}=\text{CH}_3$, OH, OBn (Bn stands for benzyl), and SPAM-1(OH:CH₃) with mixed R-groups, were obtained. Gas and vapor sorption studies (CO_2 and H_2O), and I_2 capture in liquid media for all the SPA-1(R) illustrate the influence of the R group(s) on the sorption properties of these porous materials.

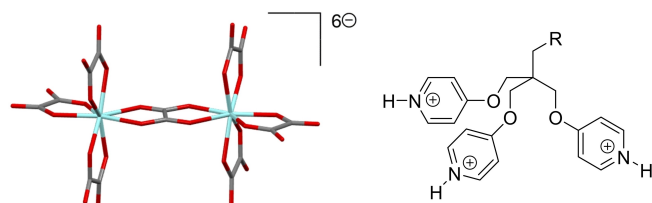
Results and discussion

Synthesis

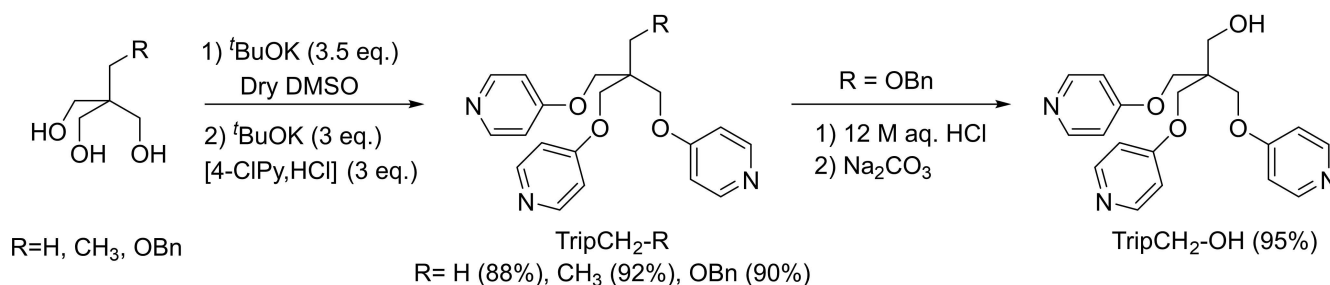
The tripodal pyridine compounds $\text{TripCH}_2\text{-R}$ with $\text{R}=\text{H}$, CH_3 and OBn have been prepared with high yields by etherification of the corresponding triol with 4-chloropyridine as outlined in Scheme 2. The alcohol derivative $\text{TripCH}_2\text{-OH}$ was obtained quantitatively from $\text{TripCH}_2\text{-OBn}$ by cleavage of the benzyl ether group in aqueous HCl (12 M). The detailed procedures and the characterization data are given in the Experimental section.

The SPA-1(R)· $x\text{H}_2\text{O}$ materials, with the general formula $[(\text{H}_3\text{-TripCH}_2\text{-R})_2\{\text{Zr}_2(\text{Ox})_7\}] \cdot x\text{H}_2\text{O}$, have been prepared for $\text{R}=\text{H}$, CH_3 , OBn and OH by reacting the appropriate $\text{TripCH}_2\text{-R}$ and $\text{K}_6[\text{Zr}_2(\text{Ox})_7]$ in 2:1 ratio in an acidic aqueous solution ($\text{pH} \approx 2$). The mixed-R SPAM-1(OH:CH₃)· $x\text{H}_2\text{O}$, of formula $[(\text{H}_3\text{-TripCH}_2\text{-OH})(\text{H}_3\text{-TripCH}_2\text{-CH}_3)\{\text{Zr}_2(\text{Ox})_7\}] \cdot x\text{H}_2\text{O}$, was obtained from the 1:1:1 mixture of the proper reagents.

These compounds were isolated as transparent crystalline solids in good yields (70–90%, Figure S1) when reaction mixtures were kept undisturbed. The time required to observe the first SPA/SPAM crystals appeared to be strongly influenced by the nature of the R group; it varied from 1 h ($\text{R}=\text{OBn}$) to 1 week ($\text{R}=\text{OH}$). It can be mentioned that for SPAM-1(OH:CH₃) the first crystals formed after about 96 h, which is intermediate to the times required for $\text{R}=\text{CH}_3$ (24 h) and $\text{R}=\text{OH}$ (1 week).



Scheme 1. Building-blocks used in the formation of porous architectures SPA-1(R) and SPAM-1(OH:CH₃): the H-bond acceptor $[\text{Zr}_2(\text{Ox})_7]^{6-}$ (left), and the H-bond donors, $(\text{H}_3\text{-TripCH}_2\text{-R})^{3+}$ tripodal cations with $\text{R}=\text{H}$, CH_3 , OBn and OH (right).



Scheme 2. Synthesis of $\text{TripCH}_2\text{-R}$ molecules ($\text{R}=\text{H}$, CH_3 , OBn, OH).

Crystal structures

Crystal structure was determined in each case by single crystal X-ray diffraction studies. All these compounds crystallize in the trigonal $R\bar{3}$ space group with half of a $[\text{Zr}_2(\text{Ox})_7]^{6-}$ metal-oxalate, one $(\text{H}_3\text{-TripCH}_2\text{-R})^{3+}$ cation, and x H_2O molecules (from $x = 0$ for $\text{R} = \text{OBn}$ to $x = 6$ for $\text{R} = \text{OH}$) in their asymmetric units (Figures S2–S6). Cell parameters, crystallographic data and structure refinement parameters are reported in Table S1.

All structures are sustained by strong ionic H-bonds involving N-H^+ groups of $(\text{H}_3\text{-TripCH}_2\text{-R})^{3+}$ cations as H-bond donors (D-H) and oxalates O atoms of $[\text{Zr}_2(\text{Ox})_7]^{6-}$ complexes as H-bond acceptors (A). These interactions are characterized by

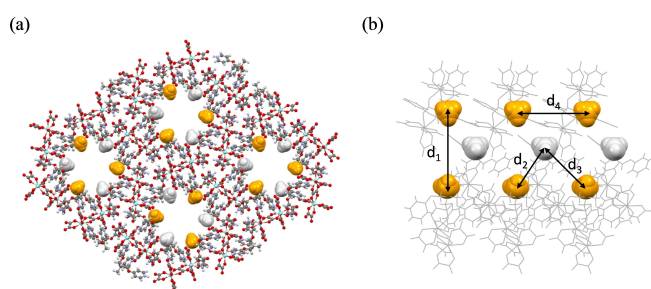


Figure 1. View of 1D channels for SPA-1(H). (a) Ball and stick representation of the supramolecular framework along c crystallographic direction. (b) Wireframe representation of sectional pore view along b showing the arrangement and distances between C atoms of CH_3 groups decorating the channels; $d_1 = 10.811$, $d_2 = 7.716$, $d_3 = 8.378$ and $d_4 = 10.124$ Å. H_2O molecules hosted in the channels are omitted. Color codes in (a): C, grey; H, light grey; Zr, light blue; N, dark blue; O, red. In (a) and (b) CH_3 groups are represented in space filling mode either in orange or in grey depending on the plane in which they are located. Additional information can be found in Figure S10.

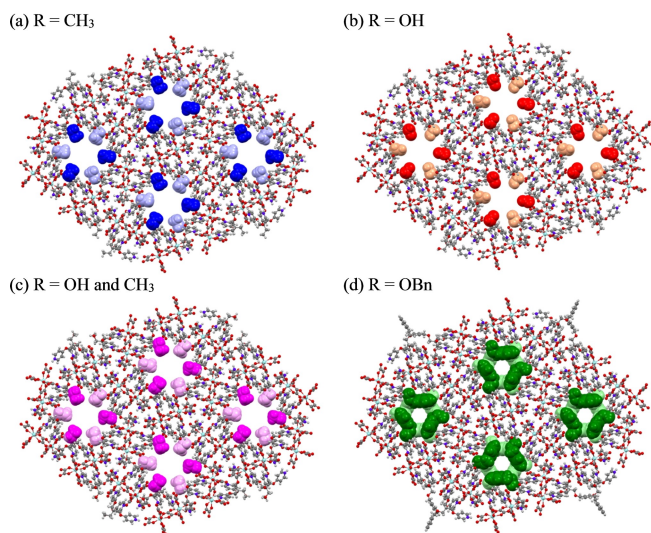


Figure 2. View of the crystal structure along the c -direction for isostructural SPA-1(R) highlighting 1D channel decoration: (a) $\text{R} = \text{CH}_3$; (b) $\text{R} = \text{OH}$; (c) $\text{R} = \text{OH}$ and CH_3 ; (d) $\text{R} = \text{OBn}$. H_2O molecules hosted in the channels are omitted. $\text{CH}_2\text{-R}$ groups are represented in space-filling mode, using dark or light color, depending on the plane they are located. Color codes: $\text{R} = \text{CH}_3$, blue; $\text{R} = \text{OH}$, red; $\text{R} = \text{OH}$ and CH_3 , violet; $\text{R} = \text{OBn}$ green; C, grey; H, light grey; N, dark blue; O, red; Zr, light blue. Space-filling representation is given in Figure S8.

$\text{D}\cdots\text{A}$, i.e. $\text{N}\cdots\text{O}$, distances between 2.621(6) and 2.833(6) Å, among the shortest found in N-H/M(oxalate) H-bonds (see Table S2 for details on H-bonds). In all cases, $(\text{H}_3\text{-TripCH}_2\text{-R})^{3+}$ cations behave as three-connecting building blocks and form H-bonds with oxygen atoms belonging to three different $[\text{Zr}_2(\text{Ox})_7]^{6-}$. Reciprocally, $[\text{Zr}_2(\text{Ox})_7]^{6-}$ units behave as six-connecting building blocks and are H-bonded with six different tris-cations (Figure S7). The interconnections between building-units result in neutral three-dimensional (3D) H-bonded frameworks showing large voids along c -axis and narrower apertures along orthogonal crystallographic directions. Mutual interpenetration of two identical frameworks occlude the latter to afford the final SPA showing infinite channels running along c direction (Figures 1 and 2, and Figure S8).

In SPAM-1($\text{OH}:\text{CH}_3$), $\text{R} = \text{OH}$ and CH_3 groups show a 1:1 statistical disorder. This observation may reveal a random distribution of $\text{R} = \text{OH}$ and $\text{R} = \text{CH}_3$ groups, or their alternation on defined crystallographic positions on the pore walls. Although crystallography cannot distinguish between these two possibilities, this result is in agreement with the 1:1 mixture of the $(\text{H}_3\text{-TripCH}_2\text{-R})^{3+}$ cations used in synthesis of this material, and with the ^1H NMR spectrum obtained for crystals of SPAM-1($\text{OH}:\text{CH}_3$) dissolved in hot D_2O (Figure S9).

A detailed examination of the channel structure for SPA-1(H) identified two sets of methyl groups (i.e., $\text{CH}_2\text{-H}$) positioned in two different planes in an offset manner (Figure 1a and Figure S10), giving the pore openings a circular appearance in the crystallographic c direction. (ca 8.5 Å in diameter^[64]). The separation between the methyl groups (i.e. $\text{C}\cdots\text{C}$) in plane and out-of plane ($d_1 = 10.81$ Å, $d_2 = 7.72$, $d_3 = 8.38$ Å and $d_4 = 10.12$ Å, Figure 1b) leads to a substantial void volume bounded by the channel walls. For SPA-1(R) with $\text{R} = \text{CH}_3$ or $\text{R} = \text{OH}$ (Figure 2), in plane shortest $\text{C}\cdots\text{C}$ and $\text{O}\cdots\text{O}$ distances between R groups are slightly reduced to $d_1 = 8.98$ Å and $d_1 = 8.51$ Å respectively, while the out of plane distances d_2 are 7.20 Å for $\text{R} = \text{CH}_3$ and to 6.53 Å for $\text{R} = \text{OH}$. For these derivatives the apparent circular pore cross sections are decreased to about 6.5 Å in diameter.^[64] With the bulkier OBn group the pore walls are upholstered by benzyl groups (Figure 2d) and the channel void is drastically reduced; the apparent pore cross section is about 3 Å in diameter for SPA-1(OBn), but the overall structure of H-bonded assembly is the same as for the other SPA-1(R).

The potential porosity (i.e. solvent accessible void versus volume of the solid) of these SPA frameworks has been estimated using Mercury;^{[65][66]} it amounts to 20.5% ($\text{R} = \text{H}$),^[61] 19.9% ($\text{R} = \text{CH}_3$), 19.0% ($\text{R} = \text{OH}$), 19.2% ($\text{R} = \text{CH}_3:\text{OH}$), and 4.0% ($\text{R} = \text{OBn}$). Views of SPA-1(R) and SPAM-1($\text{OH}:\text{CH}_3$) highlighting voids are given in Figure S11.

In freshly isolated as-synthesized materials, the channels are occupied by H_2O molecules, however, only part of them are detected from diffraction data. These are the H_2O H-bonded to the channels' wall. For a related SPA, solid state NMR revealed that some H_2O molecules are mobile in the pores and thus escape the crystallographic order probed by X-ray diffraction,^[62] it is likely that the same is true for the SPA-1 series as shown by other analytical data. The combination of structure data, TGA

(Figure S12) and chemical analyses converged to about 12 H₂O per [H₃-TripCH₂R)₂{Zr₂(Ox)₇] unit in SPA-1(R) with R=H, CH₃, OH, and mixed OH:CH₃, and to a single H₂O for R=OBn.

Evolution of crystal structures during a sorption cycle

X-ray structures of SPA-1(OH) were also investigated on the same crystal at 373 K after gradual heating under dry N₂ (HT activated phase), at 100 K after cooling down from 373 K under dry N₂ (LT activated phase), and at 100 K after the crystal was kept in air at RT for one week (i.e. fully re-hydrated). Drawings of the corresponding asymmetric units are given in Figures S13–S15, and details on crystallographic data and H-bonds are compiled in Tables S3 and S4. Crystal structures of the HT and LT activated phase reveal no major changes in the framework topology and confirm the absence of any H₂O in the channels, in agreement with the TGA and compositional analysis performed for the activated phase (see below). They also indicate that the compound exhibits a framework with permanent porosity. Comparison of the structures of the as-synthesized compound, SPA-1(OH)·12H₂O, and its LT activated phase shows that the channel aperture is only slightly altered following the departure of H₂O, with a contraction of the cell parameters by 3% along *a* and *b*. The structure of the re-hydrated phase confirms the uptake of H₂O at the single crystal level. However only a fraction of the guest molecules, i.e. 2.33 H₂O, are crystallized and evidenced in the channel, whereas the actual content for this rehydrated phase was 10.4 H₂O, as determined by thermogravimetric analysis (Figure S16).

Framework robustness

TGA supplied information on the chemical robustness of the frameworks upon thermal treatment and dehydration. Figure 3 shows the TGA traces recorded between RT and 300 °C for R=H, CH₃ and/or OH (TGA traces up to 600 °C for all SPA1-(R) are given in Figure S12). Overall, all SPA show comparable behaviors with a first weight loss consistent with dehydration of the material, a plateau reflecting the chemical robustness of the activated framework, followed by a second weight loss above 250 °C due to chemical decomposition. Clear differences in the temperature dependences of the H₂O release can be noticed (Figure 3, insert). For SPAM-1(OH:CH₃), the temperature at which dehydration is completed is between those observed for the SPA with R=OH and CH₃. The same observation is made for its decomposition temperature, which is increased by 50 °C with respect to SPA-1(OH).

Powder X-ray diffraction (PXRD) of a bulk sample for each derivative confirmed a single phase conforming to the crystal structure. This technique also established the structural robustness of the open frameworks upon dehydration. For each SPA and on the same sample, PXRD patterns were recorded at RT (i.e. as-synthesized SPA), 413 K (i.e. dehydrated), and again at RT after a stay in air at 298 K for 24 h. In all cases, the PXRD patterns are in agreement with those calculated for the crystal

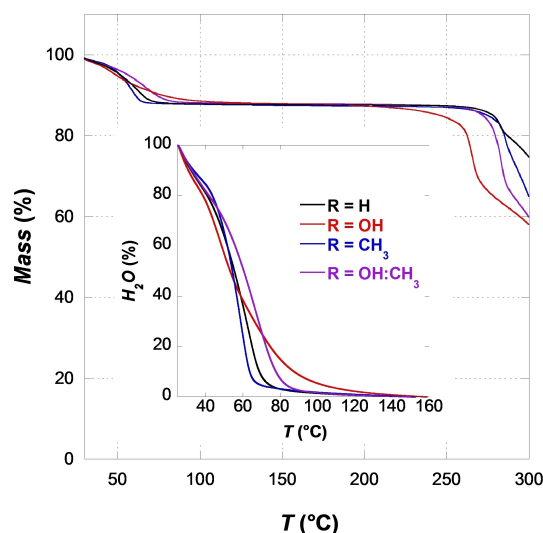


Figure 3. TGA traces for SPA-1(R) with R=H, black; R=CH₃, blue; R=OH:CH₃, violet; R=OH, red. Mass (%) and (insert) H₂O (%) hosted in the channels as a function of *T* (°C). (For SPA-1(OBn), see Figure S12 in Supporting Information).

structure obtained at 100 K for the hydrated SPAs (Figures S17 to S21), demonstrating remarkable structural robustness during a H₂O sorption cycle. Such framework rigidity upon activation and sorption of polar guest molecules is quite rare for porous HOF materials.

Gas sorption and porosity characteristics

Gas-sorption isotherms recorded after a simple activation (i.e. crystal water removal) in vacuum at RT or 373 K of the as-synthesized solids lead to poor sorption of either N₂ or CO₂.^[61] A pre-activation procedure of the SPA appeared crucial to achieve large sorption capacities. This consisted in exchanging the H₂O hosted in the channels by more volatile solvent molecules. Best results were obtained when H₂O was changed for MeOH or acetone before activation (Figure S22) leading to an adsorbed volume of CO₂ in perfect agreement with the potential of the SPA-1(R) (Table 1). The N₂ sorption study yielded a low uptake presumably due to small micropores. At the cryogenic temperature of 77 K diffusion of N₂ molecules into small micropores or ultramicropores (pores smaller than 7 Å) is very slow and may lead to under-equilibration of measured adsorption isotherms, which will give erroneous results of the analysis.^[67–68] Such problems arising from narrow pores can be eliminated by using CO₂ adsorption analysis at 195 K.^[69–71] CO₂ adsorption at this temperature versus N₂ analysis at 77 K occurs with higher diffusion rates, hence is faster and offers confidence that the adsorption points are equilibrated. In addition, owing to its larger quadrupole moment and greater polarizability, CO₂ has a stronger electrostatic interaction than N₂ with polar surfaces, leading to higher affinities and capacities of the gas in small micropores. Subsequently, materials with pores of smaller sizes,

SPA-1(R)	Porosity ^[a] (% $V_{\text{void}}/V_{\text{unit cell}}$)	Pore volume ^[b] calc. ($\text{cm}^3 \cdot \text{g}^{-1}$) ^[b]	exp. ($\text{cm}^3 \cdot \text{g}^{-1}$) ^[c]	Surface calc. ($\text{m}^2 \cdot \text{g}^{-1}$) ^[b]	exp. ($\text{m}^2 \cdot \text{g}^{-1}$) ^[d]	CO ₂ sorption ($\text{cm}^3 \cdot \text{g}^{-1}$)
R = H	20.5	0.147	0.160	425	405	89
R = CH ₃	19.9	0.144	0.135	417	357	75
R = OH	19.0	0.133	0.015	384	68	8
R = CH ₃ and OH	19.2	0.139	0.140	402	361	77
R = OBn	4.0	0.025	0.008	–	31	4

[a] Mercury void calculation;^[63,65] [b] Total pore volume or surface area calculated from the single XRD data and the void estimation; [c] Total pore volume measured at $P = 1$ atm; [d] Surface area calculated assuming a Langmuir model for the CO₂ adsorption isotherm.

that are accessible to CO₂ molecules but not to N₂ can be analyzed.^[72]

The CO₂ adsorption/desorption isotherms recorded at 195 K for SPA-1(R) with R = H, CH₃, OH, and for SPAM-1 (OH:CH₃) are given in Figure 4 (isotherm for SPA-1(OBn), can be found in Figure S23); the results are gathered in Table 1 and compared to the effective porosity characteristics of the frameworks. For all SPA-1(R) except for R = OH, CO₂ adsorption isotherms at zero pressure show a steep slope of the curve versus applied pressure due to the high affinity and strong interactions for the gas with the micropores, followed by a saturation profile above 0.2 atm. The largest volume is taken up by SPA-1(H) (89 $\text{cm}^3 \cdot \text{g}^{-1}$) as expected for the material with the smallest dangling groups in the channels. For SPA with R = CH₃ and R = OH:CH₃ the adsorbed CO₂ volumes are very similar (75 and 77 $\text{cm}^3 \cdot \text{g}^{-1}$, respectively). Very good agreements were found between the experimental pore volume and surface area, calculated from a Langmuir isotherm fitting model, and the porosity data deduced from the X-ray structures. Surprisingly, for SPA-1(OH) the adsorbed CO₂ volume (about 8 $\text{cm}^3 \cdot \text{g}^{-1}$) is small and corresponds to only 10% of the effective pore volume deduced from the crystal structure. It is comparable to that found for SPA-1(OBn) (about 4 $\text{cm}^3 \cdot \text{g}^{-1}$ at $P = 1$ atm), which

indeed has a low structural pore volume. Overall, surface areas of 405, 357, 361, 68 and 31 $\text{m}^2 \cdot \text{g}^{-1}$ were deduced from these CO₂ adsorption measurements at 195 K for R = H, CH₃, (OH:CH₃), OH and OBn respectively.

H₂O sorption

H₂O-vapor sorption isotherms (Figures 5 and S24) have been recorded to evaluate the hydrophilic character of the SPA-1(R) as a function of the R groups decorating the channel walls, except for R = OBn. All SPAs behave as hydrophilic solids, with most of the water adsorption occurring for $P/P_0 < 0.2$. For SPA-1(OH), a marked affinity for water is evidenced by a type I isotherm characterized by a steep rise up to $P/P_0 = 0.1$, followed by a smoother adsorption for higher relative pressures. Sorption isotherms showing a sigmoidal shape profile are observed for R = H, CH₃ and (OH:CH₃). The higher affinity for H₂O of channels decorated by R = H groups as compared to R = CH₃ is evidenced by the lower P/P_0 range where most of the water uptake and release occurs for SPA-1(H). According to the two kinds of R groups decorating the channels of SPAM-1(OH:CH₃), water

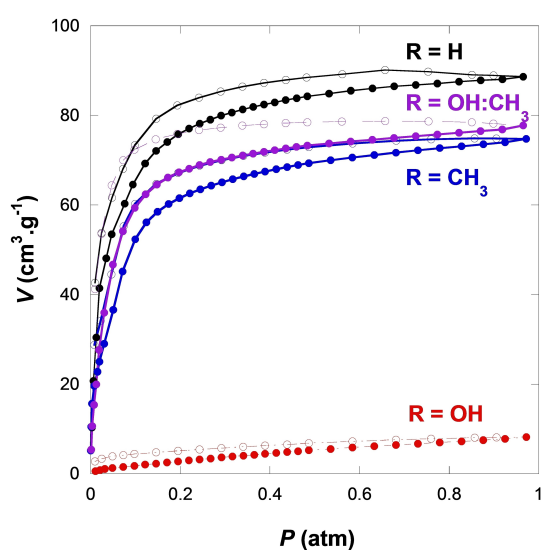


Figure 4. CO₂ adsorption (●) and desorption isotherms (○) measured at 195 K for SPA-1(R) and SPAM-1(OH:CH₃) materials. Individual adsorption-desorption isotherms, including that for R = OBn, are shown in Figure S23.

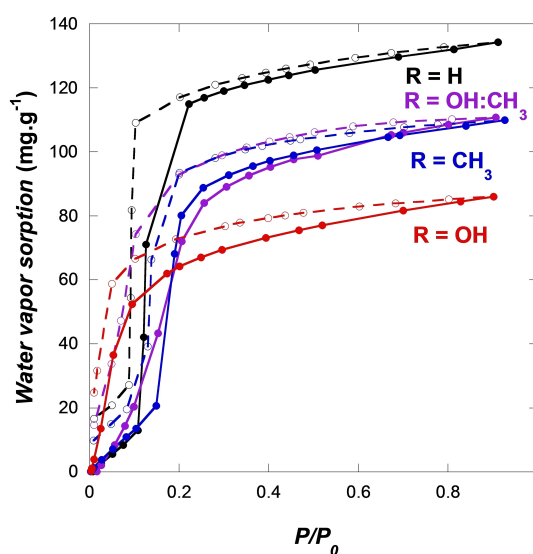


Figure 5. H₂O-vapor adsorption (full line) and desorption (dashed line) isotherms measured at 293 K for SPA-1(R). Individual adsorption-desorption isotherms are shown in Figure S24.

sorption isotherms fall between those found for SPA-1(OH) and SPA-1(CH₃). The step of water uptake for the mixed SPAM-1 is shifted to lower relative pressure compared to SPA-1(CH₃), indicating the higher hydrophilicity brought in by the OH-groups. It can be noticed that the adsorption isotherm closely follows that of SPA-1(CH₃), while desorption isotherm is closer to that of SPA-1(OH), resulting in a larger hysteresis than for the single-R materials. This study clearly shows that it is possible to fine-tune the hydrophilicity of the micropores in the SPA-1 series.

For the SPA-1(H), the total amount of H₂O re-adsorbed is in good agreement with the initial water content, i.e. 11.3 out of the 12 molecules for as-synthesized SPA. It amounts to about 80% for SPA-1(CH₃) and for SPAM-1(OH:CH₃) with 9.5 out of 12 H₂O molecules. However, for SPA-1(OH), the uptake is lower than expected with recovery of ca. 60% of the starting water content (around 7 molecules out of 12); a behavior akin to that observed for CO₂ sorption.

The fatigability of the materials, i.e. the evolution of the hydration rate after several successive adsorption cycles, was evaluated by TGA experiments. In a typical cycle, the supramolecular material was heated to 180 °C (1 °C·min⁻¹) before being slowly cooled to RT under dry N₂ atmosphere and then exposed to wet N₂. This sequence was repeated consecutively several times while H₂O sorption/desorption was followed by a gravimetric analyzer (Figure S25). The H₂O sorption was found to be fully reversible and the rate unchanged over several cycles for the SPA-1 with R=H, CH₃, and (OH:CH₃). For SPA-1(OH), approximately 7 molecules of H₂O are recovered after first sorption cycle while 12 molecules of H₂O were removed during the first activation. Sorption of these 7 molecules then turned reversible for the following cycles (Figure S25c). The amount of adsorbed H₂O remained barely changed if SPA-1(OH)·7H₂O was exposed to wet N₂ for several more hours. A water content much closer to that of the starting material, i.e. 10.4 H₂O per [Zr₂(Ox)₇]⁶⁻ out of the 11.8 H₂O molecules in the as-synthesized SPA-1(OH), was obtained when the activated SPA was kept in ambient air for 1 week (Figure S16). This suggests that the observed partial filling is not related to material damage or activation problems, but to kinetic considerations, which is confirmed by the sorption of I₂ (see below).

The crystal structure of activated SPA-1(OH) (see above) showed that the porous framework is not altered upon activation; therefore, the weak CO₂ sorption and incomplete H₂O uptake cannot be attributed to structural changes. Since the isostructural SPAM-1(OH:CH₃) adsorbs amounts of H₂O and CO₂ in agreement with the porosity of the solid, the results obtained for SPA-1(OH) must be attributed to the alcohol groups and the density of these units decorating the channel walls. The stronger interactions between these functional groups and the adsorbate may be the cause of a slowed down diffusion of the guest molecules inside the channels. A further possible origin might be a partial occlusion of the pore inlets by chemical moieties (from the building units) located at outer surface of the crystals. The OH groups in (H₃-Trip-CH₂-OH)³⁺ may contribute to H-interactions between the terminating units,

thus acting as gates limiting access to the channels; at least as long as these reversible interactions are not broken.

I₂ capture and release

The affinity of these SPA for iodine was investigated for the whole series of SPA-1(R) by immersing activated crystals in hexane solutions of I₂. In order to compare the observations, the same amount of porous solid and an identical volume of I₂ solution (of fixed concentration) were used for each derivative. Rapid discoloration of the solutions was observed for SPA with R=H, CH₃ and (OH:CH₃), while a much longer time was required to observe the same result for R=OH (Figure 6 and Figure S26). Concomitantly, the colorless crystals turned dark brown. Clearly, the fastest adsorption occurs with SPA-1(H), whereas SPA-1(CH₃) and SPAM-1(OH:CH₃) have comparable behaviors, and a much slower process is evident with SPA-1(OH). As expected, for SPA-1(OBn) the colors of the solution and crystals remain unchanged; the channels are too small to accommodate I₂. This latter observation rules out that iodine is only adsorbed on the outer surfaces of SPA crystals.

The I₂ adsorbed upon equilibration (2 weeks) amounts 0.75–0.8 I₂ per [Zr₂(Ox)₇]⁶⁻ unit. This content was determined by EA and TGA (see experimental section in Supporting Information and Figures S27–S31 for TGA traces) and is in perfect agreement with relative amount of I₂ introduced initially in each vial (a maximum of 0.85 equivalent per [Zr₂(Ox)₇]⁶⁻). Powder X-ray diffraction studies confirmed that the crystal phase of the SPA was not altered during the I₂ sorption (Figures S32–S36).

Single-crystal structure investigations were performed for all I₂@SPA-1(R) derivatives to assess the organization of the iodine molecules in the channels (Figures S37–S40). The I₂ molecules are systematically organized in hexameric units sandwiched between two sets of R groups decorating channels (Figure 6b

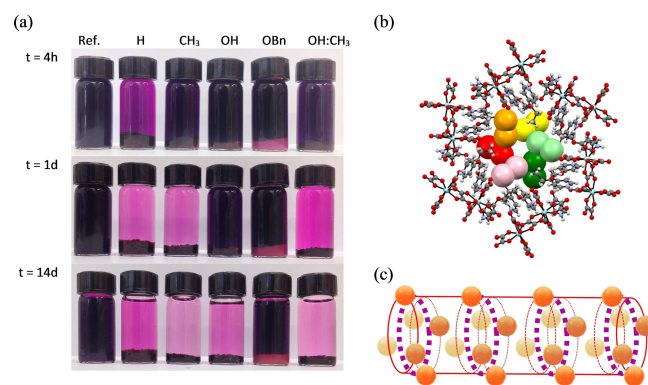


Figure 6. (a) Evolution of the coloration of the hexane solutions associated with I₂ adsorption by activated SPA-1(R) and SPAM-1(OH:CH₃) (see also Figure S26). (b) Supramolecular organization of I₂ guests in the channels of SPA-1(R), the depicted view is for R=CH₃; color code: C, grey; H, light grey; N, dark blue; O, red; Zr, light blue; I₂ molecules involved in hexameric units are shown using six different colors. (c) Relative position of I₂ hexameric units (dashed purple circle) with respect to CH₂-R groups (spheres) on pore walls. Color codes: C, grey; H, light grey; N, dark blue; O, red; Zr, light blue; I, purple.

and Figures S41–43). Their corrugated arrangement is typical for halogen-bonding interactions^[73] evidenced by short I₂...I₂ contacts (Figure S44). The iodine units also interact with the SPA framework, mainly with oxygen atoms of oxalates and weak H-bonds involving aromatic C–H groups as donors (Figure S44 for details on short contacts).^[73] The nature of the R group has no obvious effect on the crystallized I₂ arrangement but it is noticed that for R=OH a short distance is found between the alcohol O-atom and an I-atom (O231...I2_{0.66+y}, 0.33-x+y, 2.33-zr 3.80(2) Å, C23-O231-I, 123(1)°) suggesting a possible H...I bond interaction.

Adsorbed I₂ remained in the pores when the crystals were dipped in neat hexane, however, progressive release was observed when the solids were immersed in ethanol (Figure S45). Examination of the desorption process along the first minutes clearly shows it operates faster for the less polar SPA (R=H and R=CH₃) than for more polar ones (R=OH:CH₃ and R=OH). For SPA-1(H) and SPA-1(CH₃) the almost complete release of the iodine is supported by the light-brown color of the crystals. For SPAM-1(OH:CH₃) and even more for SPA-1(OH), release is more progressive and obviously not complete as shown by the deeper color of the solids. No further release was observed for crystals kept in EtOH for several weeks, suggesting that I₂ is efficiently trapped in the SPA channels and that the amount sequestered is largest for SPA-1(OH).

Conclusions

The robust ionic H-bonded assemblage scheme found in SPA-1(R) allowed the formation of a series of isostructural porous frameworks with different R groups located in the channels. SPA-1 with pore-walls decorated by polar, apolar, or mixture of both R groups have been achieved and such alterations permitted to adjust the sorption characteristics for SPA with very close porosities, as shown with CO₂ or H₂O gas sorption, and iodine in liquid media.

Pore walls decorated with two types of R groups can lead to more subtle sorption characteristics than a simple average behavior of the single R-functional referent SPAs. For instance, SPAM-1(OH:CH₃) shows I₂ and H₂O sorption rates very close to SPA-1(CH₃), while its desorption behavior is very similar to SPA-1(OH). This results in a larger hysteresis for the mixed-R SPA.

These results demonstrate that material design and pore tailoring are also possible for H-bonded porous architectures, which is particularly scarce in the field.

Experimental section

General Methods

All chemicals were purchased from commercial sources and used as received. DMSO used in the synthesis of TripCH₂-R derivatives was dried over CaH₂. Infrared spectra were recorded with a Perkin-Elmer Spectrum Two FTIR spectrometer in the range 4000–600 cm⁻¹, using the ATR mode. ¹H and ¹³C NMR were performed on a Bruker Advance 400 spectrometer. C, H, N elemental analyses were

performed by the Elemental Analyses Service of the Laboratoire de Chimie de Coordination in Toulouse using a Perkin-Elmer 2400 II CHNS/O analyzer. Acetanilide (Elemental analysis calcd (%) for C₈H₉NO, C: 71.0, H: 6.71, N: 10.36) was used as reference material for analyzer calibration. Samples were weighed on a Sartorius CPA2P microbalance with ±1 μg resolution. Samples weights ranging from 1.7 to 2.2 mg were used. The presented values are the average of two analyses. TGA measurements were done on three different instruments: (1) the as-synthesized materials were analyzed on a TGA/DSC+STAR® System (METTLER TOLEDO) in the RT–600 °C temperature range (heating rate of 1 °C·min⁻¹ between TA and 300 °C, then 10 °C·min⁻¹ up to 600 °C) under a dry N₂ flux. (2) H₂O release/uptake experiments were performed using a PERKIN-ELMER Diamond TG/DTA instrument, through a home-made adaptation of the TGA device allowing to expose activated SPA-1(R) and activated SPAM-1(OH:CH₃) samples to a wet N₂ flux. Each SPA was exposed to 4 consecutive release/uptake cycles (ca. 440 min per cycle). In a typical cycle, as synthesized sample is progressively heated from RT to 180 °C (dry N₂, 1 °C·min⁻¹, ca. 150 min), cooled back to RT (dry N₂, ca. 110 min), and exposed to wet N₂ at RT (ca. 180 min); (3) TG measurements for activated SPA/SPAM materials and I₂-loaded SPA/SPAM materials were done on a NETZSCH STA 409 PC/PG TG/DTA instrument, under a dry N₂:O₂ (3:1) flux, in the RT–600 °C temperature range; the compounds were heated using a 1 °C·min⁻¹ heating rate from RT to 600 °C.

X-ray diffraction

Single crystal X-ray diffraction: Single crystal diffraction data were collected on a Bruker Kappa APEX II diffractometer or on an Oxford Diffraction Gemini diffractometer, using molybdenum (λ = 0.71073 Å) or copper (λ = 1.54180 Å) radiation. Measurements at low and high temperature were performed using an Oxford Cryosystems Cooler Device. The structures have been solved using SUPERFLIP^[74] or SHELXS-86^[75] and refined by means of least-squares procedures on F² using the software package CRYSTALS.^[76] Atomic Scattering Factors were taken from the International tables for X-ray Crystallography.^[77] All non-hydrogen atoms (excepting H₂O molecules for (SPAM-1(OH:CH₃)·5.5H₂O)) were anisotropically refined. All hydrogen atoms were refined using a riding model. The mobility of part of the H₂O molecules hosted in the channels of the SPA-1(R) crystals induced for several structures A-level alerts during the CIF verification procedure. These alerts are associated with short distances between partially occupied atoms or with anomalous voids in the structures. These voids correspond to diffuse electron densities that cannot be reasonably attributed to fractions of H₂O molecules. As required by the CCDC, all of these alerts have been commented in the cif.

For I₂@SPA-1(R), the electronic density for the I atoms revealed a partial occupation, i.e. 0.1 (R=H),^[61] 0.5 (R=CH₃ and OH:CH₃), and 0.7 (R=OH). The low I-occupations rates observed for some derivatives results from diffraction data being collected early in the adsorption process due to increased mosaicity for longer loading times.

For SPAM-1(OH:CH₃), the LT activated phase of SPA-1(OH), and I₂@SPAM-1(OH:CH₃), the OH and/or CH₃ groups on C(23) were found to be located on two different sites with partial occupancies. Refinement of the used model led to a satisfactory solution. For the LT activated SPA-1(OH) phase, a residual density maximum larger than expected is reported near the metal. No twin or disorder could be detected. This might be due to imprecise absorption correction.

Deposition Numbers 2172371 (for SPA-1(CH₃)·8H₂O), 2172370 (for SPA-1(OBn)), 2172369 (for SPA-1(OH)·12H₂O), 2172372 (for SPAM-1(OH:CH₃)·5.5H₂O), 2172368 (for SPA-1(OH) activated_HT, 2172364

(for SPA-1(OH) activated_LT, 2172367 (for SPA-1(OH)_rehydrated), 2172366 (for I₂@SPA-1(CH₃)), 2172365 (for I₂@SPA-1(OH)) and 2172373 (for I₂@SPAM-1(OH:CH₃)) contain the supplementary crystallographic data for this paper. These data are provided free of charge by the joint Cambridge Crystallographic Data Centre and Fachinformationszentrum Karlsruhe Access Structures service. The already reported structures of SPA-1(H)·10.17H₂O and SPA-1(H)·0.2I₂ have CCDC number 993983 and 993988, respectively.^[61]

Powder X-ray diffraction: powder X-ray diffraction (PXRD) patterns were recorded on a XPert Pro (θ - θ mode) Panalytical diffractometer with $\lambda(\text{Cu}_{K\alpha 1, K\alpha 2}) = 1.54059, 1.54439 \text{ \AA}$. The high temperature PXRD patterns were recorded at 140 °C on the same apparatus. A heating rate of 2 °C min⁻¹ was used to warm the sample, and the heated sample was kept at 140 °C during 2 h previous to perform the measurements. All data were collected in the 2° < 2 θ < 40° range, with 0.02 steps and 10 s of exposure. Most part of experimental and calculated patterns are dominated by a strong diffraction peak around 2 θ = 4°; to make possible the comparison between diffractograms for higher 2 θ values, each diffractogram in Supporting Information is plotted two times, from 2 θ = 2–40° (a, normalized view), and from 2 θ = 5–40° (b, magnified view).

Sorption experiments

General procedure for activation of the SPA-1(R) materials: Crystals of as-synthesized SPA-1(R)·xH₂O were immersed in a MeOH:H₂O 2:1 mixture (1 mL per 20 mg of crystals) during 24 h. After this time, supernatant solution was removed and replaced by same volume of anhydrous MeOH, which was regenerated every 12 h during 3 days. MeOH was finally removed and resulting pre-activated crystals activated under vacuum at RT during 24 h before being engaged in sorption experiments.

H₂O vapor phase sorption: Measurements were conducted on a Quantachrome VStar4 in the relative pressure range of P/P₀ = 0–0.9. Samples were activated prior to the measurement using the same activation procedure as described above.

N₂ and CO₂ sorption measurements: Gas adsorption isotherms were recorded on evacuated materials on a Micromeritics ASAP 2020 analyzer. Samples were pre-activated as described above and degassed without heating in vacuum (10⁻⁵ hPa) for at least 12 h. CO₂ adsorption experiments were recorded at 195 K with dry ice in acetone. Specific surface areas were deduced from the CO₂ adsorption isotherms by fitting the experimental data with a Langmuir model in the relative pressure range P/P₀ from 0 to 1, and assuming a molecular surface of CO₂ equal to 0.17 nm².

I₂ sorption: 0.133 mmol batches of hydrated SPA and SPAM (ca 230 mg of as-synthesized materials) are smashed and activated (see above) prior to be introduced in 4 mL vials containing I₂ solution in hexane (C = 2.84 × 10⁻² mol L⁻¹, ca. 0.114 mmol of I₂ per vial). The samples used for characterizations (IR, PXRD, TG and EA) were kept in the hexane solutions for 3 weeks to 1 month to allow equilibration. Single crystals used for SCXRD experiments were obtained following same methodology starting from single crystals (50 mg batches in 4 mL vials; C = 2.84 × 10⁻² mol L⁻¹ for I₂ solution in hexane); the exposure times of the different activated SPA-1(R) to I₂ solutions ranged from 1 week (R = H) to 3 weeks (R = OH).

Synthesis and characterizations

Synthesis of K₆[Zr₂(Ox)₇]·4H₂O: The synthesis was adapted from a reported procedure.^[78] A solution of ZrOCl₂·8H₂O (1.289 g; 4 mmol) in 40 mL of distilled water is added dropwise to a mixture of K₂C₂O₄·1H₂O (1.480 g; 8 mmol) and H₂C₂O₄·2H₂O (1.008 g; 8 mmol)

dissolved in 80 mL of the same solvent. The resulting clear solution is stirred during 30 min, transferred in a 250 mL glass crystallizing dish and left for slow evaporation at room temperature. First crystals appear after 2 weeks. After one month, large colorless crystals of K₆[Zr₂(Ox)₇]·4H₂O are recovered by filtration, washed with 10 mL of iced water and dried in air. Yield: 80% (1.770 g; 1.6 mmol). IR (ATR-FT, diamond): 3414 (br), 1711 (s), 1688 (vs), 1508 (w), 1394 (s), 1268 (m), 1197 (w), 988 (w), 908 (m), 810 (s), 797 (s), 652 (m) cm⁻¹; Elemental analysis calcd (%) for C₁₄H₈O₃₂Zr₂K₆·(K₆[Zr₂(Ox)₇]·4H₂O): C 15.21, H 0.73; found: C 15.28, H 0.85.

Synthesis of 1,1,1-trishydroxymethyl-2-benzyloxyethane

This molecule is prepared at several grams scale starting from pentaerythritol and following a multistep procedure described in literature.^[79] ¹H NMR (400 MHz, DMSO-d₆): δ = 7.28 (m, 5H), 4.44 (s, 2H), 4.23 (t, 3H), 3.42 (d, 6H), 3.37 ppm (s, 2H); ¹³C NMR (400 MHz, DMSO-d₆): δ = 139.4, 128.6, 127.6, 127.5, 72.9, 69.8, 61.3, 46.1 ppm; IR (ATR, germanium): 3301 (s), 2862 (w), 1628 (w), 1472 (w), 1364 (s), 1027 (vs) cm⁻¹; Elemental analysis calcd (%) for C₁₂H₁₈O₄: C 63.70, H 8.02; found: C 63.72, H 8.04.

General synthetic procedure for TripCH₂-R molecules with R = H, CH₃ and OBn

TripCH₂-H (R = H):^[80] 1,1,1-trishydroxymethylethane (1.826 g; 15.2 mmol) is dissolved in dry DMSO (35 mL). A first fraction of tBuOK (5.966 g; 53.2 mmol) is added as a solid. The resulting yellowish suspension is stirred at room temperature during 1 h. A second fraction of tBuOK (5.114 g; 45.6 mmol) is added. It is immediately followed by addition of 4-chloropyridinium chloride (6.480 g; 45.6 mmol) as a solid. The reaction mixture turns brown and viscous. It is warmed at 60 °C during 72 h. After cooling to RT, TripCH₂-H is precipitated as a white solid by adding the reaction mixture to 1.5 L of distilled water. The solid is recovered by filtration, washed several times with distilled water, and dried in air. Water free sample is recovered through recrystallization using a minimum amount of boiling MeOH:THF (2:8) solvent mixture. Yield: 88% (4.71 g; 13.4 mmol). ¹H NMR (400 MHz, DMSO-d₆): δ = 8.34 (d, 6H), 6.99 (d, 6H), 4.16 (s, 6H), 1.25 ppm (s, 3H); ¹³C NMR (400 MHz, CDCl₃): δ = 164.6, 151.1, 110.2, 69.8, 40.1, 17.1 ppm; IR (ATR, germanium): 3034 (w), 2982 (w), 2948 (w), 2872 (w), 1587 (s), 1569 (s), 1501 (m), 1466 (m), 1456 (m), 1418 (m), 1384 (w), 1337 (w), 1280 (s), 1239 (m), 1206 (s), 1044 (s), 1015 (s), 996 (s), 846 (s), 813 (s) cm⁻¹; Elemental analysis calcd (%) for C₂₀H₂₁N₃O₃, (TripCH₂-H): C 68.36, H 6.02, N 11.96; found: C 68.54, H 6.07, N 11.79.

TripCH₂-CH₃ (R = CH₃): This molecule is obtained by following a synthetic procedure similar to that used to obtain TripCH₂-H, but starting from 1,1,1-trishydroxymethylpropane (2.038 g; 15.2 mmol). Yield: 92% (5.12 g; 14 mmol). ¹H NMR (400 MHz, DMSO-d₆): δ = 8.35 (d, 6H), 6.99 (d, 6H), 4.17 (s, 6H), 1.74 (q, 2H), 0.94 ppm (t, 3H); ¹³C NMR (400 MHz, DMSO-d₆): δ = 164.8, 151.4, 110.9, 67.8, 42.5, 23.0, 7.9 ppm; IR (ATR, germanium): 3048 (w), 3028 (w), 2980 (w), 2940 (w), 2882 (w), 1592 (vs), 1568 (m), 1499 (m), 1471 (m), 1418 (m), 1283 (vs), 1207 (m), 1062 (m), 1035 (vs), 1000 (w), 989 (w), 861 (s), 839 (s), 815 (vs), 778 (w) cm⁻¹; Elemental analysis calcd (%) for C₂₁H₂₃N₃O₃, (TripCH₂-CH₃): C 69.02, H 6.34, N 11.50; found: C 69.09, H 6.35, N 11.47.

TripCH₂-OBn (R = OBn): TripCH₂-OBn is obtained by following a synthetic procedure similar to that used to obtain TripCH₂-H, but starting from 1,1,1-trishydroxymethyl-2-benzyloxyethane (3.437 g; 15.2 mmol) as a starting triol. Yield: 90% (6.270 g; 13.7 mmol). ¹H NMR (400 MHz, DMSO-d₆): δ = 8.36 (d, 6H), 7.22 (m, 5H), 6.97 (d, 6H), 4.50 (s, 2H), 4.25 (s, 6H), 3.70 ppm (s, 2H); ¹³C NMR (400 MHz,

DMSO- d_6): δ = 164.6, 151.3, 138.5, 128.6, 127.9, 127.7, 110.9, 72.9, 67.6, 66.3, 44.7 ppm; IR (ATR-FT, diamond): 3061 (w), 3030 (w), 2949 (w), 2886 (w), 1692 (w), 1589 (vs), 1570 (m), 1500 (m), 1464 (w), 1419 (w), 1366 (w), 1279 (vs), 1211 (vs), 1166 (w), 1098 (m), 1027 (m), 990 (w), 860 (w), 841 (m), 816 (s), 740 (m), 700 (m) cm^{-1} ; Elemental analysis calcd (%) for $\text{C}_{27}\text{H}_{27}\text{N}_3\text{O}_4$, (TripCH₂-OBn): C 70.88, H 5.95, N 9.18; found: C 70.76, H 6.05, N 9.17.

Synthesis of TripCH₂-OH (R = OH)

A solution TripCH₂-OBn (5,032 g; 11 mmol) in aqueous HCl (12 M, 10 mL) is stirred at room temperature for 12 h. Benzyl chloride generated during the reaction is extracted using chloroform (three times 30 mL). The aqueous phase is diluted with 10 mL of distilled water and pH adjusted to 8 by careful addition of solid Na₂CO₃ resulting in precipitation of TripCH₂-OH. The solid is collected by filtration, washed several times with water and dried in air. Recrystallization in MeOH:THF (2:8) leads to water-free TripCH₂-OH (3.858 g; 10.5 mmol; Yield: 95%). ¹H NMR (400 MHz, DMSO- D_6): δ = 8.36 (d, 6H), 6.98 (d, 6H), 5.04 (t, 1H), 4.21 (s, 6H), 3.70 ppm (d, 2H); ¹³C NMR (400 MHz, DMSO- D_6): δ = 164.8, 151.4, 110.9, 66.2, 59.0, 45.2 ppm; IR (ATR-FT, diamond): 3182 (br), 3053 (w), 3033 (w), 2952 (w), 2888 (w), 1594 (vs), 1569 (m), 1503 (m), 1465 (m), 1425 (w), 1285 (vs), 1210 (m), 1058 (m), 1045 (m), 1030 (vs), 999 (w), 990 (w), 866 (m), 839 (m), 825 (s), 815 (m) cm^{-1} ; Elemental analysis calcd (%) for $\text{C}_{20}\text{H}_{21}\text{N}_3\text{O}_4$, (TripCH₂-OH): C 65.38, H 5.76, N 11.44; found: C 65.29, H 5.73, N 11.38.

General synthesis and characterizations of SPA-1(R) and SPAM-1 (OH:CH₃) materials

R = H: [(H₃-TripCH₂-H)₂Zr₂(Ox)₇] · 12H₂O, SPA-1(H) · 12H₂O.^[80]

TripCH₂-H (218 mg, 0.62 mmol) is suspended in 6 mL of distilled water. Dissolution and formation of (H₃-TripCH₂-H)³⁺ cation is achieved by dropwise addition of concentrated aqueous HCl until pH ≈ 2. (K₆[Zr₂(C₂O₄)₇] · 4H₂O) (0.344 g; 0.31 mmol) is dissolved in the same volume of water at pH ≈ 2 and added dropwise to the (H₃-TripCH₂-H)³⁺ solution. The resulting clear solution is let undisturbed. Crystals suitable for X-ray diffraction studies are observed after 48 h and after two weeks 379 mg (0.22 mmol, Y = 72%) of colorless crystalline SPA-1(H) are isolated. IR (ATR-FT, diamond): 3422 (br), 3082 (w), 3017 (w), 2942 (w), 2891 (w), 1709 (w), 1676 (vs), 1646 (s), 1595 (w), 1513 (m), 1467 (w), 1404 (m), 1305 (m), 1290 (m), 1271 (w), 1203 (m), 1187 (w), 1033 (m), 1017 (m), 993 (w), 903 (w), 833 (m), 807 (m), 791 (m) cm^{-1} ; TGA: weight loss calcd for 12 H₂O: 12.5%; Expected weight loss is observed at 150 °C. See Figure S12(a) in the Supporting Information for TGA trace; Elemental analysis calcd (%) for $\text{C}_{54}\text{H}_{72}\text{N}_6\text{O}_{46}\text{Zr}_2$, [(H₃-TripCH₂-H)₂Zr₂(Ox)₇] · 12H₂O: C 37.63, H 4.21, N 4.88; found: C 37.79, H 4.13, N 4.83.

The SPA-1(R) with R = CH₃, OBn, OH, and OH:CH₃, were prepared following the synthesis procedure used to obtain SPA-1(H); details can be found in the Supporting Information.

Supporting Information

Experimental, crystallographic data, additional views and information on crystal structures, PXRD, TGA, CO₂ and H₂O sorption isotherms, I₂ absorption and release experiments, are given for all SPA-1(R).

Author contribution

Nans Roques: Conceptualization, methodology, investigation, synthesis, data analyses, writing. Anthony Tovar-Molle: synthesis. Carine Duhayon: crystal structure studies. Stephane Brandès: CO₂ sorption investigations, writing. Alex Spieß and Christoph Janiak: H₂O-sorption studies and writing. Jean-Pascal Sutter: Conceptualization, methodology, coordination, writing and editing.

Acknowledgments

The authors are grateful to Mrs. Maritie Garnier-Carrière and M. Dominique Stein for their contributions to the synthesis of some precursors, and to Dr. Laure Vendier and Mr. Jean-François Meunier for technical assistance in analytical data recording.

Conflict of Interest

The authors declare no conflict of interest.

Data Availability Statement

The data that support the findings of this study are available from the corresponding author upon reasonable request.

Keywords: crystal engineering · hydrogen bonds · host-guest systems · microporous materials · supramolecular chemistry

- [1] P. Li, M. R. Ryder, J. F. Stoddart, *Acc. Mater. Res.* **2020**, *1*, 77–87.
- [2] M. Mastalerz, I. M. Oppel, *Angew. Chem. Int. Ed.* **2012**, *51*, 5252–5255; *Angew. Chem.* **2012**, *124*, 5345–5348.
- [3] I. Hisaki, N. Ikenaka, E. Gomez, B. Cohen, N. Tohrai, A. Douhal, *Chem. Eur. J.* **2017**, *23*, 11611–11619.
- [4] B. Han, H. Wang, C. Wang, H. Wu, W. Zhou, B. Chen, J. Jiang, *J. Am. Chem. Soc.* **2019**, *141*, 8737–8740.
- [5] B. Yu, L. Li, S. Liu, H. Wang, H. Liu, C. Lin, C. Liu, H. Wu, W. Zhou, X. Li, T. Wang, B. Chen, J. Jiang, *Angew. Chem. Int. Ed.* **2021**, *60*, 8983–8989.
- [6] J. Gao, Y. Cai, X. Qian, P. Liu, H. Wu, W. Zhou, D.-X. Liu, L. Li, R.-B. Lin, B. Chen, *Angew. Chem. Int. Ed.* **2021**, *60*, 2–9; *Angew. Chem.* **2021**, *133*, 2–2.
- [7] X. Zhang, J.-X. Wang, L. Li, J. Pei, R. Krishna, H. Wu, W. Zhou, G. Qian, B. Chen, B. Li, *Angew. Chem. Int. Ed.* **2021**, *60*, 10304–10310.
- [8] Z. Sun, Y. Li, L. Chen, X. Jing, Z. Xie, *Cryst. Growth Des.* **2015**, *15*, 542–545.
- [9] E. Gomez, Y. Suzuki, I. Hisaki, M. Moreno, A. Douhal, *J. Mater. Chem. C* **2019**, *7*, 10818–10832.
- [10] G. Xing, T. Yan, S. Das, T. Ben, S. Qiu, *Angew. Chem. Int. Ed.* **2018**, *57*, 5345–5349; *Angew. Chem.* **2018**, *130*, 5443–5447.
- [11] P. Tholen, C. A. Peebles, R. Schaper, C. Bayraktar, T. S. Erkal, M. M. Ayhan, B. Çoşut, J. Beckmann, A. O. Yazaydin, M. Wark, G. Hanna, Y. Zorlu, G. Yücesan, *Nat. Commun.* **2020**, *11*, 3180.
- [12] E. Gomez, M. Gutiérrez, B. Cohen, I. Hisaki, A. Douhal, *J. Mater. Chem. A* **2018**, *6*, 6929–6939.
- [13] Q. Yin, P. Zhao, R.-J. Sa, G.-C. Chen, J. Lü, T.-F. Liu, R. Cao, *Angew. Chem. Int. Ed.* **2018**, *57*, 7691–7696; *Angew. Chem.* **2018**, *130*, 7817–7822.
- [14] J. Luo, J.-W. Wang, J.-H. Zhang, S. Lai, D.-C. Zhong, *CrystEngComm* **2018**, *20*, 5884–5898.
- [15] R.-B. Lin, Y. He, P. Li, H. Wang, W. Zhou, B. Chen, *Chem. Soc. Rev.* **2019**, *48*, 1362–1389.
- [16] B. Wang, R.-B. Lin, Z. Zhang, S. Xiang, B. Chen, *J. Am. Chem. Soc.* **2020**, *142*, 14399–14416.

- [17] T.-H. Chen, I. Popov, W. Kaveevivitchai, Y.-C. Chuang, Y.-S. Chen, O. Daugulis, A. J. Jacobson, O. Š. Miljanić, *Nat. Commun.* **2014**, *5*, 5131.
- [18] I. Hisaki, C. Xin, K. Takahashi, T. Nakamura, *Angew. Chem. Int. Ed.* **2019**, *58*, 11160–11170; *Angew. Chem.* **2019**, *131*, 11278–11288.
- [19] T. Khadivjam, H. Che-Quang, T. Maris, Z. Ajoyan, A. J. Howarth, J. D. Wuest, *Chem. Eur. J.* **2020**, *26*, 7026–7040.
- [20] M. A. Little, A. I. Cooper, *Adv. Funct. Mater.* **2020**, *30*, 1909842.
- [21] A. Pulido, L. Chen, T. Kaczorowski, D. Holden, M. A. Little, S. Y. Chong, B. J. Slater, D. P. McMahon, B. Bonillo, C. J. Stackhouse, A. Stephenson, C. M. Kane, R. Clowes, T. Hasell, A. I. Cooper, G. M. Day, *Nature* **2017**, *543*, 657–664.
- [22] M. I. Hashim, H. T. M. Le, T.-H. Chen, Y.-S. Chen, O. Daugulis, C.-W. Hsu, A. J. Jacobson, W. Kaveevivitchai, X. Liang, T. Makarenko, O. Š. Miljanić, I. Popovs, H. V. Tran, X. Wang, C.-H. Wu, J. I. Wu, *J. Am. Chem. Soc.* **2018**, *140*, 6014–6026.
- [23] K. Ma, P. Li, J. H. Xin, Y. Chen, Z. Chen, S. Goswami, X. Liu, S. Kato, H. Chen, X. Zhang, J. Bai, M. C. Wasson, R. R. Maldonado, R. Q. Snurr, O. K. Farha, *Cell Rep. Phys. Sci.* **2020**, *1*, 100024.
- [24] B. Wang, X.-L. Lv, J. Lv, L. Ma, R.-B. Lin, H. Cui, J. Zhang, Z. Zhang, S. Xiang, B. Chen, *Chem. Commun.* **2020**, *56*, 66–69.
- [25] Y. Suzuki, M. Gutiérrez, S. Tanaka, E. Gomez, N. Tohnai, N. Yasuda, N. Matubayasi, A. Douhal, I. Hisaki, *Chem. Sci.* **2021**, *12*, 9607–9618.
- [26] A. L. Sisson, V. D. Sanchez, G. Magro, A. M. E. Griffin, S. Shah, J. P. H. Charmant, A. P. Davis, *Angew. Chem. Int. Ed.* **2005**, *44*, 6878–6881; *Angew. Chem.* **2005**, *117*, 7038–7041.
- [27] R. Natarajan, L. Bridgland, A. Sirilcukajorn, J.-H. Lee, M. F. Haddow, G. Magro, B. Ali, S. Narayanan, P. Strickland, J. P. H. Charmant, A. G. Orpen, N. B. McKeown, C. G. Bezzu, A. P. Davis, *J. Am. Chem. Soc.* **2013**, *135*, 16912–16925.
- [28] D. V. Soldatov, I. L. Moudrakovski, J. A. Ripmeester, *Angew. Chem. Int. Ed.* **2004**, *43*, 6308–6311; *Angew. Chem.* **2004**, *116*, 6468–6471.
- [29] C. H. Görbitz, *Chem. Eur. J.* **2007**, *13*, 1022–1031.
- [30] A. Comotti, S. Bracco, G. Distefano, P. Sozzani, *Chem. Commun.* **2009**, 284–286.
- [31] H. Furukawa, K. E. Cordova, M. O’Keeffe, O. M. Yaghi, *Science* **2013**, *341*, 974.
- [32] F. Ragon, H. Chevreau, T. Devic, C. Serre, P. Horcajada, *Chem. Eur. J.* **2015**, *21*, 7135–7143.
- [33] C. T. Lollar, J.-S. Qin, J. Pang, S. Yuan, B. Becker, H.-C. Zhou, *Langmuir* **2018**, *34*, 13795–13807.
- [34] Z. Ji, H. Wang, S. Canossa, S. Wuttke, O. M. Yaghi, *Adv. Funct. Mater.* **2020**, *30*, 2000238.
- [35] P. J. Waller, F. Gándara, O. M. Yaghi, *Acc. Chem. Res.* **2015**, *48*, 3053–3063.
- [36] C. S. Diercks, O. M. Yaghi, *Science* **2017**, *355*, eaal1585.
- [37] T. Steiner, *Angew. Chem. Int. Ed.* **2002**, *41*, 48–76; *Angew. Chem.* **2002**, *114*, 50–80.
- [38] K. T. Holman, A. M. Pivovar, J. A. Swift, M. D. Ward, *Acc. Chem. Res.* **2001**, *34*, 107–118.
- [39] G. Mouchaham, N. Roques, A. Kaiba, P. Guionneau, J. P. Sutter, *CrystEngComm* **2010**, *12*, 3496–3498.
- [40] W. Yang, A. Greenaway, X. Lin, R. Matsuda, A. J. Blake, C. Wilson, W. Lewis, P. Hubberstey, S. Kitagawa, N. R. Champness, M. Schroeder, *J. Am. Chem. Soc.* **2010**, *132*, 14457–14469.
- [41] M. Morshedi, M. Thomas, A. Tarzia, C. J. Doonan, N. G. White, *Chem. Sci.* **2017**, *8*, 3019–3025.
- [42] S. A. Boer, M. Morshedi, A. Tarzia, C. J. Doonan, N. G. White, *Chem. Eur. J.* **2019**, *25*, 10006–10012.
- [43] S. Yu, G.-L. Xing, L.-H. Chen, T. Ben, B.-L. Su, *Adv. Mater.* **2020**, *32*, 2003270.
- [44] T. Adachi, M. D. Ward, *Acc. Chem. Res.* **2016**, *49*, 2669–2679.
- [45] N. G. White, *Dalton Trans.* **2019**, *48*, 7062–7068.
- [46] A. D. Burrows, C. W. Chan, M. M. Chowdhry, J. E. McGrady, D. M. P. Mingos, *Chem. Soc. Rev.* **1995**, *24*, 329–339.
- [47] D. S. Reddy, S. Duncan, G. K. H. Shimizu, *Angew. Chem. Int. Ed.* **2003**, *42*, 1360–1363; *Angew. Chem.* **2003**, *115*, 1398–1402.
- [48] A. M. Beatty, *Coord. Chem. Rev.* **2003**, *246*, 131–143.
- [49] F. Thétiot, C. Duhayon, T. S. Venkatakrishnan, J.-P. Sutter, *Cryst. Growth Des.* **2008**, *8*, 1870–1877.
- [50] C.-C. Wang, C.-T. Yeh, Y.-T. Cheng, I. H. Chen, G.-H. Lee, W.-J. Shih, H.-S. Sheu, V. E. Fedorov, *CrystEngComm* **2012**, *14*, 4637–4643.
- [51] Z.-H. Zhu, H.-L. Wang, H.-H. Zou, F.-P. Liang, *Dalton Trans.* **2020**, *49*, 10708–10723.
- [52] S. A. Dalrymple, G. K. H. Shimizu, *J. Am. Chem. Soc.* **2007**, *129*, 12114–12116.
- [53] P. Dechambenoit, S. Ferlay, N. Kyritsakas, M. W. Hosseini, *J. Am. Chem. Soc.* **2008**, *130*, 17106–17113.
- [54] S. Takamizawa, T. Akatsuka, T. Ueda, *Angew. Chem. Int. Ed.* **2008**, *47*, 1689–1692; *Angew. Chem.* **2008**, *120*, 1713–1716.
- [55] G. A. Hogan, N. P. Rath, A. M. Beatty, *Cryst. Growth Des.* **2011**, *11*, 3740–3743.
- [56] I. Imaz, G. Mouchaham, N. Roques, S. Brandès, J.-P. Sutter, *Inorg. Chem.* **2013**, *52*, 11237–11243.
- [57] G. Mouchaham, M. Gualino, N. Roques, C. Duhayon, S. Brandès, J.-P. Sutter, *CrystEngComm* **2015**, *17*, 8906–8914.
- [58] I. Imaz, A. Thillet, J.-P. Sutter, *Cryst. Growth Des.* **2007**, *7*, 1753–1761.
- [59] G. Mouchaham, N. Roques, I. Imaz, C. Duhayon, J.-P. Sutter, *Cryst. Growth Des.* **2010**, *10*, 4906–4919.
- [60] G. Mouchaham, N. Roques, S. Brandès, C. Duhayon, J.-P. Sutter, *Cryst. Growth Des.* **2011**, *11*, 5424–5433.
- [61] N. Roques, G. Mouchaham, C. Duhayon, S. Brandès, A. Tachon, G. Weber, J. P. Bellat, J.-P. Sutter, *Chem. Eur. J.* **2014**, *20*, 11690–11694.
- [62] G. Mouchaham, N. Roques, W. Khodja, C. Duhayon, Y. Coppel, S. Brandès, T. Fodor, M. Meyer, J.-P. Sutter, *Chem. Eur. J.* **2017**, *23*, 11818–11826.
- [63] W. Khodja, V. Collière, M. L. Kahn, N. Roques, J.-P. Sutter, *Chem. Eur. J.* **2019**, *25*, 13705–13708.
- [64] **Note.** These values are estimated considering that R groups in the same plane are located at the vertices of an equilateral triangle and considering Van der Waals radii of C (for R=H and CH₃) and O (for R=OH). The following formula has been used: Pore diameter = $(d_1 - 2R_{vdw}) \times (2\sqrt{3})/3$.
- [65] C. F. Macrae, I. Sovago, S. J. Cottrell, P. T. A. Galek, P. McCabe, E. Pidcock, M. Platings, G. P. Shields, J. S. Stevens, M. Towler, P. A. Wood, *J. Appl. Crystallogr.* **2020**, *53*, 226–235.
- [66] **Note:** Volum outlined by rolling a sphere with radius 1.2 Å (the volum of a H₂O molecule); grid point are separated by about 0.2 Å.
- [67] J. Rouquerol, F. Rouquerol, K. S. W. Sing, P. Llewellyn, G. Maurin, *Adsorption by Powders and Porous Solids: Principles, Methodology and Applications*, Academic Press **2014**.
- [68] M. Thommes, K. Kaneko, A. V. Neimark, J. P. Olivier, F. Rodriguez-Reinoso, J. Rouquerol, K. S. W. Sing, *Pure Appl. Chem.* **2015**, *87*, 1051–1069.
- [69] J. Garrido, A. Linares-Solano, J. M. Martin-Martinez, M. Molina-Sabio, F. Rodriguez-Reinoso, R. Torregrosa, *Langmuir* **1987**, *3*, 76–81.
- [70] D. Cazorla-Amorós, J. Alcañiz-Monge, A. Linares-Solano, *Langmuir* **1996**, *12*, 2820–2824.
- [71] J. García-Martínez, D. Cazorla-Amorós, A. Linares-Solano, in *Studies in Surface Science and Catalysis, Vol. 128* (Eds.: K. K. Unger, G. Kreysa, J. P. Baselt), Elsevier, **2000**, pp. 485–494.
- [72] A. Bhunia, I. Boldog, A. Möller, C. Janiak, *J. Mater. Chem. A* **2013**, *1*, 14990–14999.
- [73] C. Laurence, J. Graton, M. Berthelot, M. J. El Ghomari, *Chem. Eur. J.* **2011**, *17*, 10431–10444.
- [74] L. Palatinus, G. Chapuis, *J. Appl. Crystallogr.* **2007**, *40*, 786–790.
- [75] A. Altomare, G. Casciaro, C. Giacovazzo, A. Guagliardi, *J. Appl. Crystallogr.* **1993**, *26*, 343–350.
- [76] P. W. Betteridge, J. R. Carruthers, R. I. Cooper, K. Prout, D. J. Watkin, *J. Appl. Crystallogr.* **2003**, *36*, 1487.
- [77] A. J. C. Wilson, in *International Tables for X-ray Crystallography Vol. C*, Dordrecht, **1992**.
- [78] R. Baggio, M. T. Garland, M. Pereg, *Inorg. Chem.* **1997**, *36*, 3198–3200.
- [79] T. J. Dunn, W. L. Neumann, M. M. Rogic, S. R. Woulfe, *J. Org. Chem.* **1990**, *55*, 6368–6373.
- [80] **Note.** An alternative synthesis procedure for this compound has been reported previously (see Ref. [61]).

Manuscript received: June 22, 2022
Accepted manuscript online: August 4, 2022
Version of record online: August 31, 2022